The Formation of the Yucatan Current Based on Observations of Summer 1971

ROBERT L. MOLINARI

NOAA Atlantic Oceanographic and Meteorological Laboratories, Miami, Fla. 33149

2 January 1975 and 15 January 1976

ABSTRACT

Temperature, salinity and Lagrangian current data collected during the summer of 1971 in the western Caribbean Sea are employed to evaluate the ageostrophic components of the flow in the formation region of the Yucatan Current. The ratio of tangential and centripetal accelerations to Coriolis acceleration for data averaged over 24 h periods remain less than 10% except in two areas. An anticyclonic turn, centered at 19°30'N, 86°W, has the largest centripetal accelerations, and in the region of Cozumel Island significant tangential accelerations occur. The large-scale accelerations and additional evidence support the hypothesis that inertial effects dominate in the formation of the Yucatan Current.

1. Introduction

The Yucatan Current is considered the first segment of the Gulf Stream system, in the sense that current speeds similar to those measured further downstream are first observed in this region. Recent studies by Molinari (1975) and Molinari and Kirwan (1975) suggest that inertial effects dominate in the formation of the Yucatan Current.

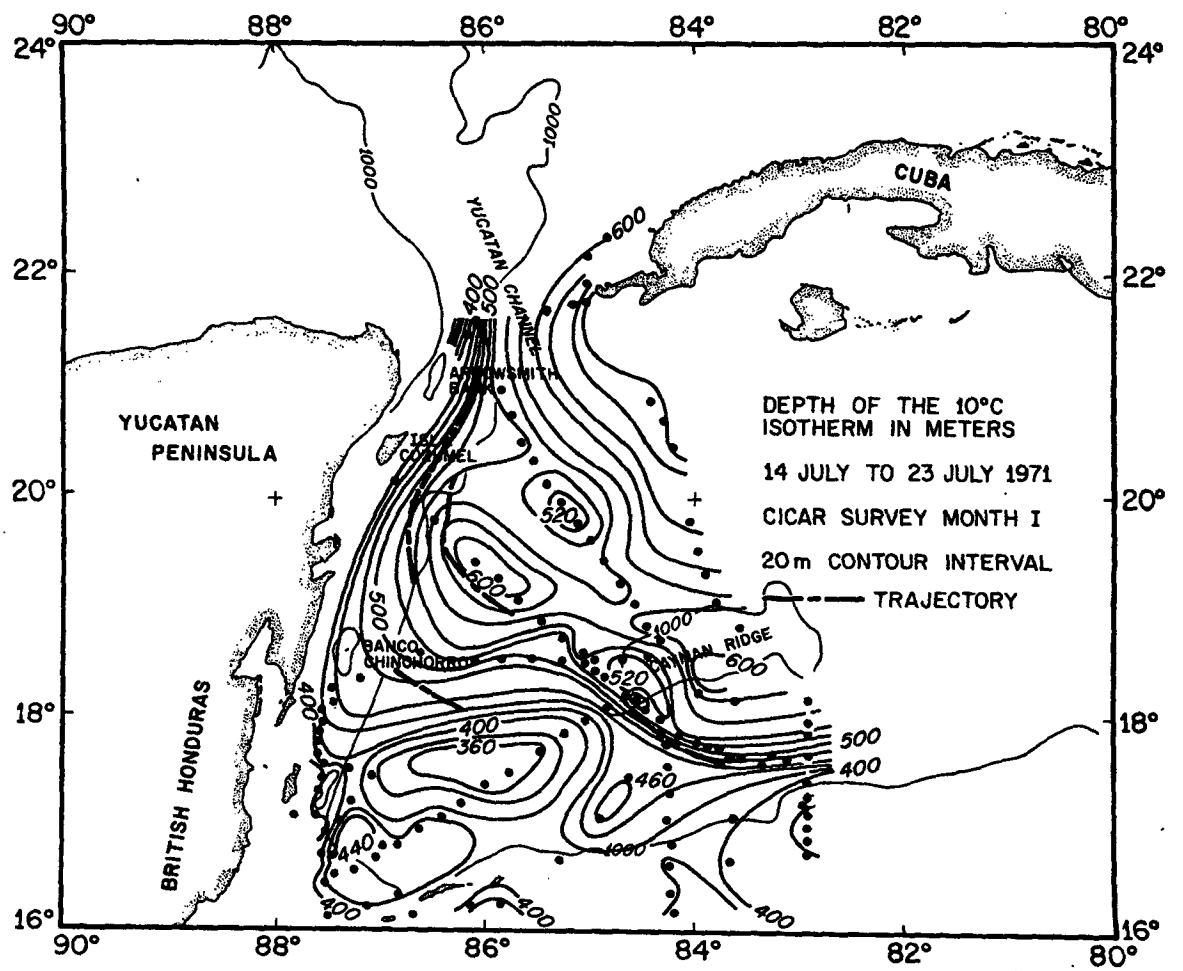

FIG. 1. The depth (m) of the 10°C isotherm, during the interval A, 14 to 23 July, 1971. The station locations are indicated by solid circles. Trajectories for the center of mass of buoy triads are also shown (see text).

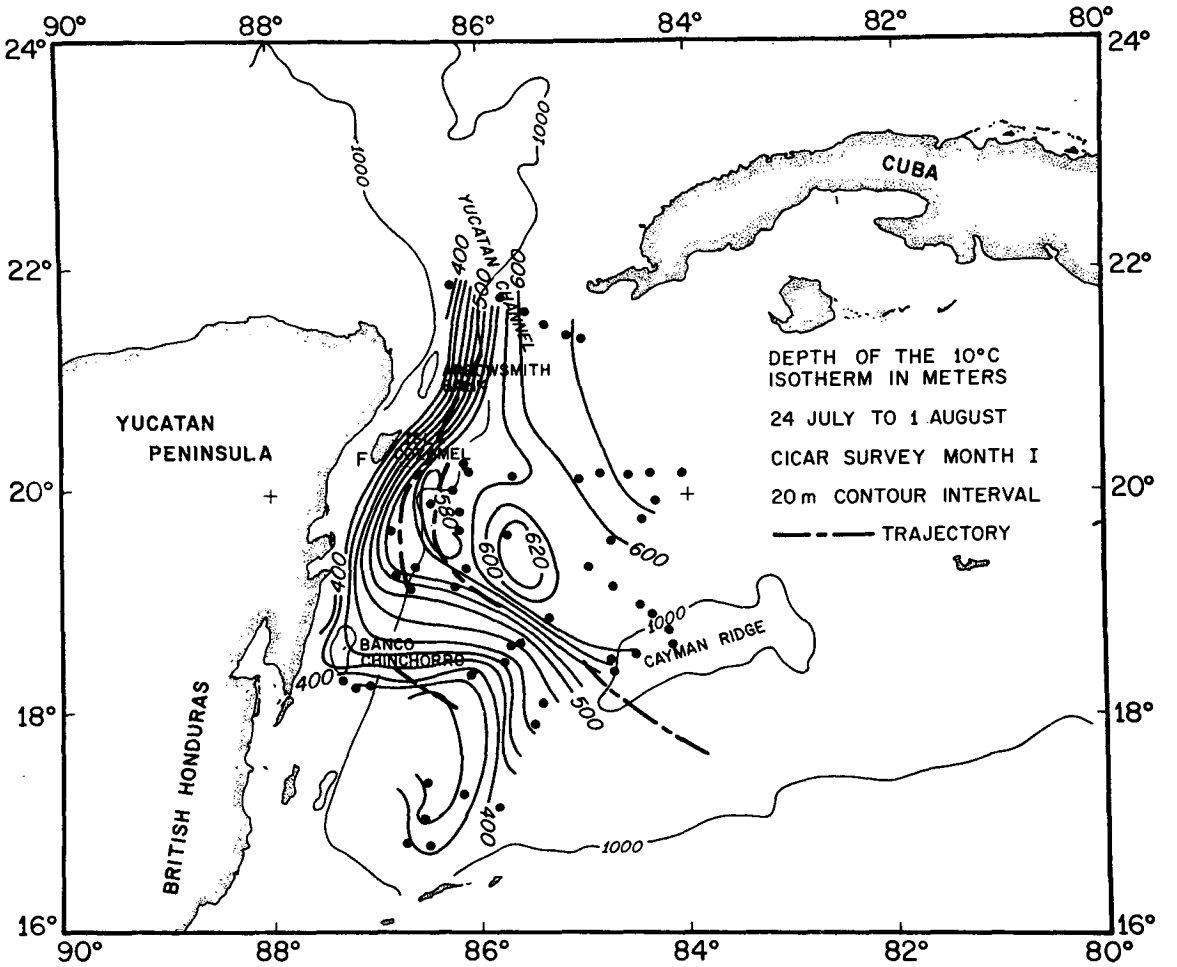

FIG. 2. As in Fig. 1, except for the interval B, 24 July to 1 August, 1971.

A two-ship operation was conducted in the summer of 1971 to investigate the formation of the Yucatan Current, and in particular to determine the nature and extent of the ageostrophic component in the western Caribbean Sea (Fig. 1) where the Current forms. In this field study, the ageostrophic component of the flow was determined by measuring the acceleration of water parcels tagged by drift buoys.

The surface buoy was described by Molinari (1973); nominally it senses the motion of the water at 40 m by a parachute drogue. Data reduction techniques, and the reduced surface drifter, temperature and salinity data collected by the NOAA ship *Researcher* were also discussed by Molinari (1973). These data, supplemented by additional temperature data collected by *Discoverer* (Hazelworth and Starr, 1975) are used in the following sections to describe the formation of the Yucatan Current in the summer of 1971.

2. Temperature-salinity data

Certain isotherm topographies are useful surrogates for the density distribution in this area. In particular, Molinari (1975) found that the 10°C topography closely maps the geostrophic current regime in the western portion of the Caribbean Sea. The study period, 14 July to 22 August, 1971, is divided into three time intervals. The intervals are selected to provide spatial resolution of the temperature field over the shortest time span. Figs. 1–3 show the 10°C topographies during these intervals (identified as A, B, C).

The 10°C topography at 83°W (Fig. 1) has a slope at 18°N consistent with a narrow and fast geostrophic current. The maximum slope occurs along a band bounded by the 460 m and 520 m contours. The band extends continuously from 83°W, 18°N to the Yucatan Strait. The acceleration along this band is not monotonic. Rather, the direction of and gradients along the band vary, suggesting accelerations, decelerations and meanderings of the current.

The temperature structure indicates the presence of eddies on either side of the maximum slope. The flows around these eddies are both cyclonic and anticyclonic. Figs. 1 and 2 suggest that there is a south to north

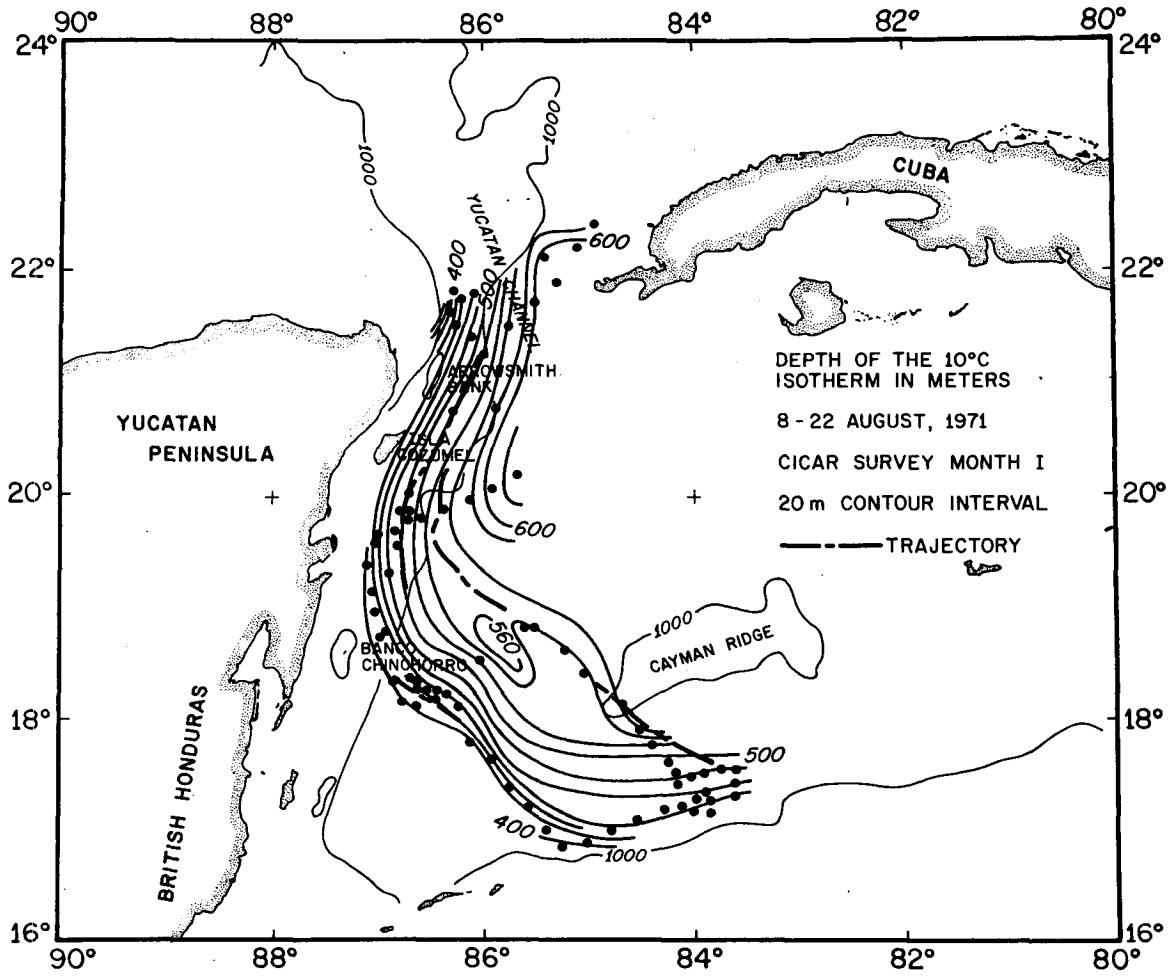

FIG. 3. As in Fig. 1, except for the interval C, 8 to 22 August, 1971.

decrease in eddy size, with no resolvable eddies found at the Yucatan Strait.

The migrations of the 460 to 520 m band show the temporal changes which occur in the main current. The only significant temporal variability occurs in the southern basin where the large eddy initially centered at 17°30′N, 86°W (Fig. 1) apparently drifts to the west. There is no significant movement of the band at the Yucatan Strait during the six-week time period.

3. Drifter data

The technique for reducing the drifter data was described by Molinari (1973) and Molinari and Kirwan (1975). This procedure provides geographic positions every 2h. The individual drogue trajectories are shown in Fig. 4.

Four sets of trajectories were obtained, and with at least three drifters being deployed in each set. Legs 1 and 2 employed the same buoys which drifted unattended from points 4 to 5 during an emergency port call. The buoys were retrieved at the end of leg 2, and redeployed in an unsuccessful attempt to sample the cyclonic flank of the current (leg 3). After a schedulep port call leg 4 was initiated, and then prematurely terminated when a storm threatened the operations area.

The results of the drifter analysis are presented below in increasing order of the derivatives of the buoy coordinate-vs-time functions, i.e., trajectories, speeds and accelerations. Finally, the ageostrophic components of the flow, as evaluated from the drifter data, are discussed.

a. Trajectories

Trajectories are computed for the center of mass of the buoy triads, and are given in Figs. 1–3. The current fields inferred from these trajectories are very similar to the circulation fields inferred from the 10°C topographies. For instance, in the Yucatan Strait region the trajectories closely follow the depth contours of the 10°C isothermal surface during all three time intervals. However, in the southern basin the trajectories parallel only those contours obtained concurrently, i.e., the leg 1 trajectory parallels the phase 1 temperature field

(Fig. 1), and the leg 4 trajectory parallels the phase 3 temperature field (Fig. 3). This result is consistent with the temporal variability observed in the tempera ture field and discussed above.

Visual inspection of the trajectories in Fig. 4 indicates that large-amplitude meanders did not occur in the area. The largest curvature in the trajectories occurs in the anticyclonic turn indicated in the temperature fields at 19°30′N, 86°W (Figs. 1–3). The average anticyclonic radius of curvature from points 7 to 10 shown in Fig. 4 is 75 km.

b. Speeds and accelerations

Buoy speeds have been computed from the position data by using a centered difference approximation to the differential. The accelerations have been computed in natural coordinates, i.e., downstream s, crossstream n (positive to the left of the downstream axis), and vertical z (positive up). The accelerations are tangential (dV/dt), centripetal (KV^2) and Coriolis (fV), where $d(\ )/dt=\partial(\ )/\partial t+V\partial(\ )/\partial s$, V is the measured speed, K the horizontal curvature (positive for downstream cyclonic turning), and f the Coriolis parameter.

The trends in the individual buoy speeds have been determined by fitting in a least-squares sense a cubic polynomial in time to the speed values. The fitted polynomial trend has been subtracted from the observed values to arrive at residual speed curves. The speed and residual speed curves for each drifter, and the polynomial fit curve for one drifter, are given in Fig. 5.

The large-scale accelerations inferred from the temperature data are apparent in the fitted polynomial curves. For instance, the temperature gradients of the anticyclonic turn centered at 19°30′N, 86°W suggest a deceleration in the flow. This deceleration occurs at 206/1930 (Fig. 5), as the drifters enter this turn. The temperature gradients increase as do the buoy speeds (leg 3, 210/0315 to 213/1315), as the drifters approach the Yucatan Strait. The largest average downstream accelerations occur in the vicinity of and north of Cozumel Island, where the speeds approach those observed in the Gulf Stream. These large-scale accelerations occur on time scales of days and/or space scales of hundreds of kilometers.

Smaller time and/or space scale disturbances are superimposed on these large-scale features. In Fig. 5, the speed curves with the trends removed show that the amplitude of these oscillations are relatively constant

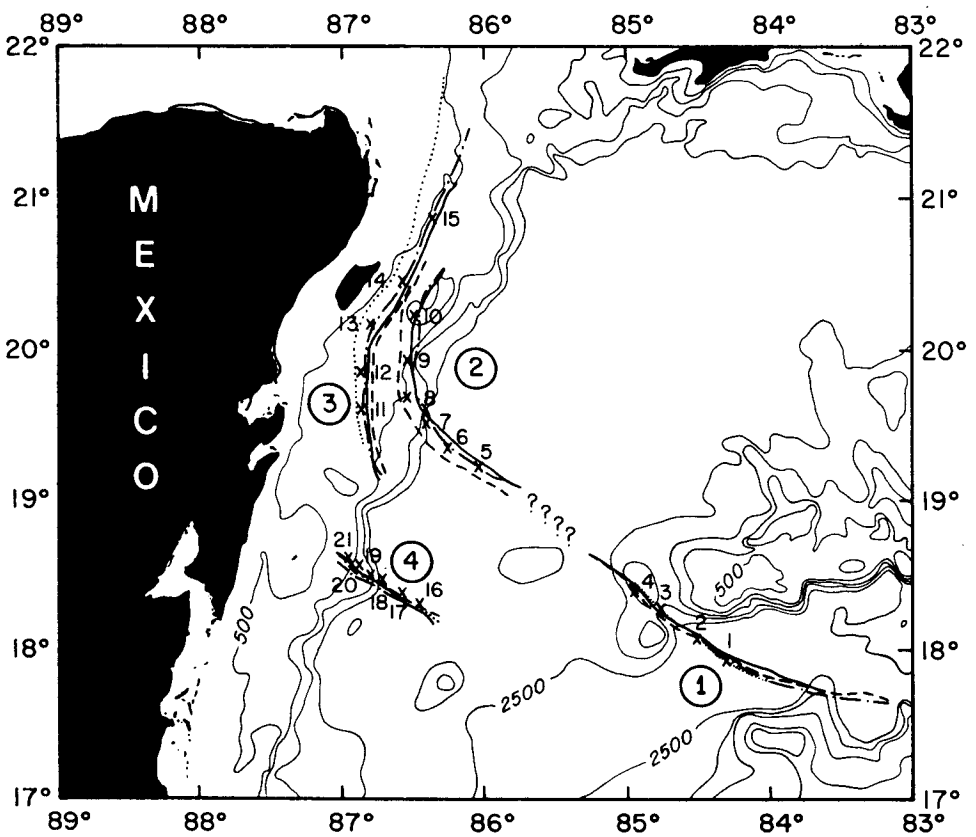

FIG. 4. Drogue trajectories as determined from 2 h positions. The trajectory of buoy 2 is continuous during legs 1 and 2 (identified by circled numbers), although the buoy was not continuously tracked from interval 4 to 5. The first and last position times (Julian day/hour) are: leg 1, 200/1830 to 204/1630; leg 2, 205/1930 to 209/0730; leg 3, 210/0315 to 213/1315; and leg 4, 228/1600 to 232/1000.

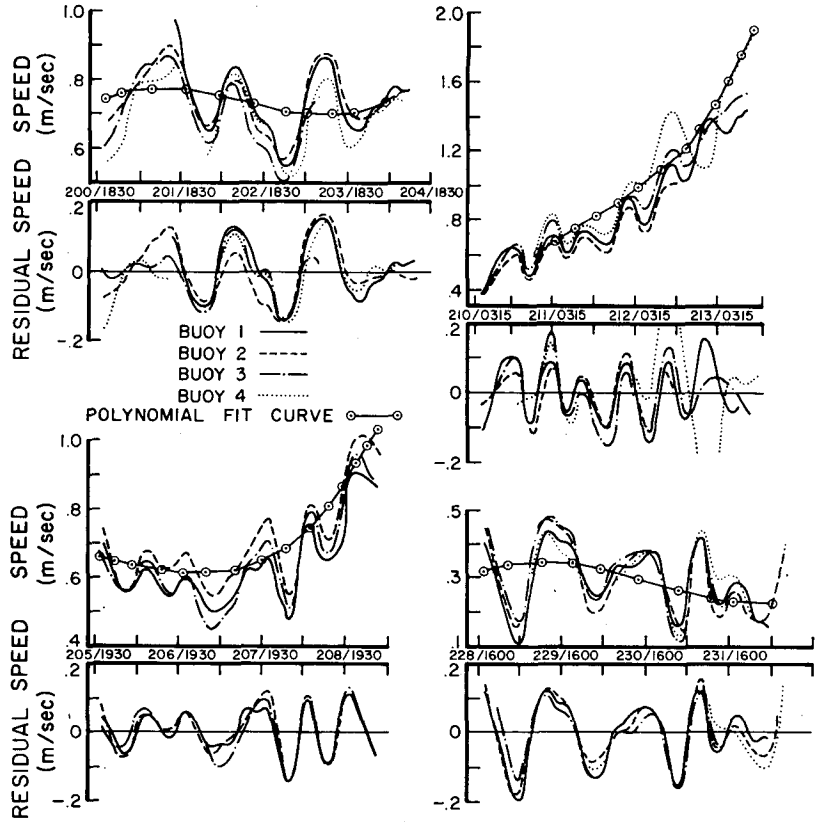

FIG. 5. The observed and residual speed curves for the trajectories of Fig. 4 as a function of time (Julian day/hour). The residual speeds are determined by subtracting the third-degree polynomial fit curve (a representative curve is shown in the upper panels of each time interval) from the observed curve.

throughout the basin, although their primary period appears to vary. A visual inspection of the records indicates that the principal period in the southern speed data is 24 h, and in the northern data, 12 h.

As indicated, no large-amplitude meanders, similar to Gulf Stream meanders, appear in the trajectory data (Fig. 4). Thus, the velocity oscillations discussed above occur along the axis of the flow, rather than normal to it. The downstream spatial extent of the oscillations vary from approximately 25 km in the low-speed regions to 75 km in the high-speed region of the basin.

c. Ageostrophic components

The horizontal equations of motion can be written in natural coordinates as

$$\frac{dV}{dt}+\frac{\partial D}{\partial s}=R_1, \tag{1}$$

$$KV^2+fV+\frac{\partial D}{\partial n}=R_2, \tag{2}$$

where D is the dynamic height relative to a level of no motion, and R_1 and R_2 include all the forcing and retarding functions. In a frictionless system the ageostrophic components are the centripetal acceleration KV^2 and the tangential acceleration dV/dt.

The terms on the left-hand side of (1) and (2) are evaluated for those portions of the trajectories where density data are available. Dynamic heights are computed relative to 600 m, since the majority of the hydrographic casts were to this depth. Accelerations for the center of mass trajectories and the density gradients are averaged over 24 h periods to eliminate the small-scale oscillations shown in Fig. 5. Table 1 lists these average properties at 12 h intervals.

If $R_2=0$, Eq. (2) becomes the gradient equation. The gradient balance expressed in percentages as $[R_2/(KV^2+fV)]\times 100$ was maintained on the average to within 10% durings legs 1, 2 and 3. The gradient balance computed relative to 600 m was not maintained during leg 4 for undetermined reasons (although internal wave aliasing of the density field may be a cause).

The terms in (1) are an order of magnitude less than the terms in (2) and therefore more difficult to evaluate realistically. However, the large-scale tangential accelerations are consistent with downstream pressure gradients observed during legs 2 and 3 (Fig. 4).

TABLE 1. Ageostrophic and geostrophic components averaged over 24 h periods.

Fig. 4 point	Time Julian day/hour	V (cm s^{-1})	fV (cm s$^{-2}\times10^4$)	$\partial D/\partial n$ (cm s$^{-2}\times10^4$)	$\lvert KV^2\rvert/fV$ $\times100$ (percent)	$\lvert dV/dt\rvert/fV$ $\times100$ (percent)
1	202/1330	0.69	0.31	0.27	8	2
2	203/0130	0.68	0.30	0.25	11	2
3	203/1330	0.71	0.32	0.31	6	4
4	204/0130	0.71	0.33	0.36	7	3
5	206/0830	0.61	0.28		10	4
6	206/2030	0.58	0.27		9	4
7	207/0830	0.58	0.28	0.20	12	3
8	207/2030	0.61	0.30	0.22	17	10
9	208/0830	0.69	0.34	0.28	12	8
10	208/2030	0.76	0.38		7	3
11	211/0215	0.66	0.32		4	3
12	211/1415	0.75	0.37	0.29	13	4
13	212/0215	0.94	0.47	0.34	8	13
14	212/1415	1.15	0.59	0.50	1	8
15	213/0215	1.49	0.70		1	7
16	229/0500	0.32	0.14		2	5
17	229/1700	0.33	0.15		9	4
18	230/0500	0.30	0.14		3	1
19	230/1700	0.29	0.13		7	3
20	231/0500	0.28	0.13		9	8
21	231/1700	0.26	0.12		0	6

The data listed in Table 1 verify the results described qualitatively in previous sections; that is, the large-scale flow undergoes little acceleration in the mid-basin (points 1–4, Fig. 4), the largest centripetal accelerations occur in the anticyclonic turn centered at 19°30′N, 86°W (point 8, Fig. 4), and the largest accelerations occur in the vicinity of Cozumel Island (point 13, Fig. 4). If $R_1=R_2=0$, the large-scale flow is geostrophic to within 20%. In particular, although the average velocity more than doubles from points 11 to 15 (Fig. 4), the maximum value of the ratio $[(dv/dt)/fV]\times100$ is only 13%.

If the ageostrophic components are evaluated for intervals of monotonically accelerating or decelerating flow (Fig. 5), the ratios of ageostrophic to geostrophic terms are considerably higher than those listed in Table 1. For instance, over these shorter averaging intervals the centripetal acceleration is as large as one-third the Coriolis acceleration, and the tangential acceleration is as large as one-fourth the Coriolis acceleration.

4. Discussion

For the average accelerations listed in Table 1, the balances expressed in (1) and (2) are confirmed qualitatively for (1), and quantitatively for (2). Molinari and Kirwan (1975) demonstrate qualitatively that potential vorticity is conserved for portions of legs 2 and 3 (points 5–9 and 11–15, Fig. 4). In addition, the absolute value of their relative vorticity is approximately 40% of the value of the planetary vorticity on the northern portion of these trajectories.

The 1971 measurements also suggest that if lateral friction plays a role in the formation process of the Yucatan Current it is limited to a narrow band along the Yucatan Peninsula. A frictional boundary layer can be characterized by a cyclonic shear zone, but the westernmost buoy of leg 3 (Fig. 4) exhibits the highest speeds measured (Fig. 5), indicating the buoys are in the anticyclonic zone of the current. The only indication that the buoys may be on the cyclonic flank of the current occur as this buoy drifts over Arrowsmith Bank. However, it is difficult to ascertain if the speed reduction is a local effect of the bank topography, or if the buoy has indeed crossed the speed axis. The proceding results provide additional support for the contention of Molinari (1975) that inertial effects dominate in the formation of the Yucatan Current.

The 24 h average ageostrophic components listed in Table 1 are seldom greater than 10% of the Coriolis accelerations. As discussed, if shorter averaging periods are used the ratio of ageostrophic to geostrophic components increases. The effect of these smaller scale features on the formation process are still matters for speculation. Plausible explanations are wind and/or tidal forcing of the upper layers. For instance, the dominant semi-diurnal and diurnal periods of the speed oscillations (Fig. 5), their constant amplitude throughout the basin, and the predominantly downstream orientation of these disturbances suggested a tidal modulation of the flow. However, the results of a tidal analysis performed on the data were inconclusive.

Acknowledgments. The invaluable assistance in the collection of data of the officers and crew of the *Researcher* is gratefully acknowledged.

The data analysis was facilitated by the programming of Mr. A. Herman, and the efforts of Mr. D. Tidwell. The figures were drafted by the publication and presentation group of Mr. R. L. Carrodus.

This work was supported in part by the National Science Foundation, under International Decade of Ocean Exploration Grant AG-253.

REFERENCES

Hazelworth, J., and R. B. Starr, 1975: Oceanographic conditions in the Caribbean Sea during the summer of 1971. NOAA Tech. Rep. ERL 344-AOML 20, 144 pp.

Molinari, R. L., 1973: Data from the Lagrangian current measurement project conducted aboard the NOAA ship *Researcher* during CICAR Survey Month I. NOAA Tech. Memo. ERL-AOML-19, 81 pp.

——, 1975: A comparison of observed and numerically simulated circulation in the Cayman Sea. *J. Phys. Oceanogr.*, **5**, 51–62.

——, and A. D. Kirwan, 1975: Calculation of differential kinematic properties from Lagrangian observations in the western Caribbean Sea. *J. Phys. Oceanogr.*, **5**, 483–491.